Article

In Silico Discovery and Subsequent Characterization of Potent 4R-Tauopathy Positron Emission Tomography Radiotracers

Published as part of the Journal of Medicinal Chemistry virtual special issue "Diagnostic and Therapeutic Radiopharmaceuticals".

Thomas J. A. Graham,* Anton Lindberg, Junchao Tong, Jeffrey S. Stehouwer, Neil Vasdev, Robert H. Mach, and Chester A. Mathis

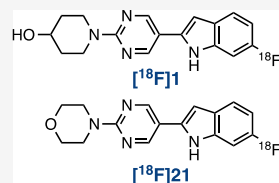Read Online

ACCESS | Metrics & More | Article Recommendations | Supporting Information

ABSTRACT: A chemical fingerprint search identified Z3777013540 (1-(5-(6-fluoro-1*H*-indol-2-yl)pyrimidin-2-yl)-piperidin-4-ol; **1**) as a potential 4R-tau binding ligand. Binding assays in post-mortem Alzheimer's disease (AD), progressive supranuclear palsy (PSP), and corticobasal degeneration (CBD) brain with [^{3}H]**1** provided K_D (nM) values in AD = 4.0, PSP = 5.1, and CBD = 4.5. *In vivo* positron emission tomography (PET) imaging in rats with [^{18}F]**1** demonstrated good brain penetration

- high affinity for 4R-tau aggregates (K_D's < 5 nM)
- high selectivity vs. amyloid-beta and alpha-synuclein aggregates
- highly brain penetrant

4R-tau positron emission tomography radiotracers

and rapid clearance from normal brain tissues. A subsequent molecular similarity search using **1** as the query revealed an additional promising compound, Z4169252340 (4-(5-(6-fluoro-1*H*-indol-2-yl)pyrimidin-2-yl)morpholine; **21**). Binding assays with [^{3}H]**21** provided K_D (nM) values in AD = 1.2, PSP = 1.6, and CBD = 1.7 and lower affinities for binding aggregated α-synuclein and amyloid-beta. PET imaging in rats with [^{18}F]**21** demonstrated a higher brain penetration than [^{18}F]**1** and rapid clearance from normal brain tissues. We anticipate that **1** and **21** will be useful for the identification of other potent novel 4R-tau radiotracers.

INTRODUCTION

The accumulation of tau protein as ordered filaments arranged in beta-pleated sheets represents an important characteristic of neurodegenerative disorders known as the tauopathies.[1−3] Human tau comprises six isoforms that possess three microtubule-binding repeats (3R) or four repeats (4R). Ordered filaments found in tauopathies vary in their makeup: Pick's disease (PiD) primarily comprises 3R-tau,[4,5] progressive supranuclear palsy (PSP) and corticobasal degeneration (CBD) are primarily 4R-tau,[4] and Alzheimer's disease (AD) and chronic traumatic encephalopathy (CTE) are made up of mixed 3R/4R-tau.[6−10] Recently, cryo-EM studies have further demonstrated that these tauopathies can be delineated by their structures. The mixed 3R/4R tauopathies (AD/CTE) share a common fold,[11−13] whereas the predominately 3R or 4R tauopathies (PiD, PSP, or CBD) comprise unique folds.[14−16] Additionally, the structures observed in AD, CTE, PSP, CBD, and PiD revealed the presence of two filament types made up of identical protofilaments.[17] Taken together, the structures of tau filaments observed in neurodegenerative tauopathies show a wide diversity.

Definitive diagnoses for all tauopathies rely on clinical presentation and post-mortem pathological examination. Over the past decade, significant progress has been made toward the development of positron emission tomography (PET) tracers for AD tauopathies. Several radiopharmaceuticals have been

advanced to investigational human AD studies, and current work is focused on improving binding affinity and selectivity for 3R/4R-tau aggregates, increasing dynamic range, and reducing nonspecific and off-target binding. Of the tau-PET radiopharmaceuticals currently under investigation, [^{18}F]-Tauvid (a.k.a. [^{18}F]flortaucipir and [^{18}F]T807) and [^{18}F]MK-6240 (Figure 1) are the most established, with the former receiving FDA approval in 2020 for patients with AD.[18−25] While both of these probes have seen investigational use for the assessment of tau pathology in AD, their potential for use in non-AD tauopathies appears to be limited. A combination of clinical and preclinical data suggest that these tracers share a common binding site on AD-tau (3R/4R) and lack evidence of high-affinity, displaceable binding to non-AD tauopathies in autoradiography experiments.[26−29] In contrast to AD-tau radioligands, PET imaging agents for 3R- and 4R-dominant non-AD tauopathies (PiD, PSP, and CBD) remain underdeveloped. Of the radioligands reported to bind 4R non-AD tauopathies, [^{18}F]PM-PBB3 (a.k.a. [^{18}F]florzolotau and
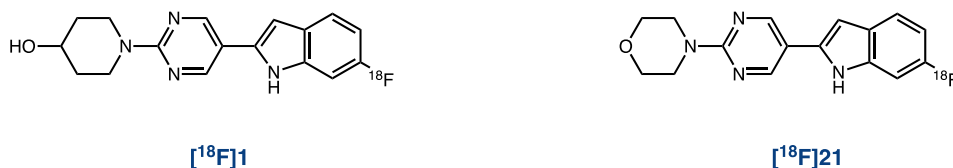
Previous work:
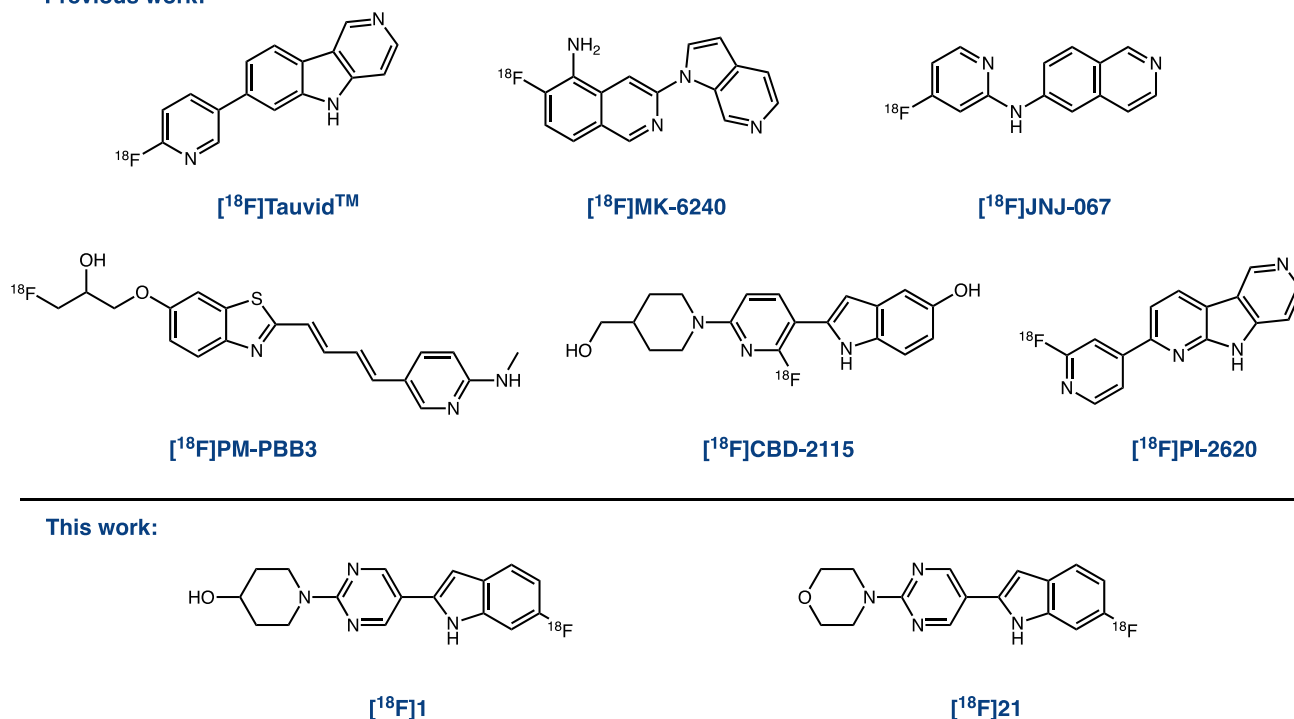
This work:

Figure 1. Structures of leading tau-PET ligands Tauvid, [18F]MK-6240, [18F]JNJ-067, [18F]PI-2620, [18F]PM-PBB3, [18F]CBD-2115, and tracers discovered in this work ([18F]1 and [18F]21).

[18F]APN-1607) and [18F]PI-2620 are the most advanced (Figure 1). Preclinical investigation of these ligands with autoradiography demonstrated that these ligands bind both AD (3R/4R) and non-AD 4R tauopathies.[30,31] Furthermore, human imaging studies with [18F]PI-2620 and [18F]PM-PBB3 show that they may be capable of detecting 4R-tau deposits in non-AD tauopathies.[31−35] While encouraging, the PET outcome measures (SUVR or DVR) of these radioligands in non-AD tauopathies were modest, and the tracers require further characterization before entering routine clinical use.[36,37]

We recently reported 2-(2-fluoro-6-(4-(hydroxymethyl)-piperidin-1-yl)pyridin-3-yl)-1H-indol-5-ol, CBD-2115 (a.k.a. OXD-2115, Figure 1), as a first in class 4R-tau ligand for PET imaging. In our assays, [3H]CBD-2115 bound AD, PSP, and CBD post-mortem tissues with high affinity.[38] While [3H]CBD-2115 showed promising in vitro results, the low brain penetrance of [18F]CBD-2115 in nonhuman primates and rodents likely prevents its use as a radiotracer for in vivo PET studies. Furthermore, it is anticipated that additional improvements to the binding affinity for 4R-tau aggregates will be required as a consequence of their low abundance in non-AD tauopathies relative to the higher abundance of 3R/4R aggregates typically found in AD cases. This notion is further supported by the modest PET outcome measures observed with [18F]PI-2620 and [18F]PM-PBB3. Given the promising in vitro binding results of [3H]CBD-2115 for non-AD tauopathies, the current study was initiated to identify chemical matter that may improve the affinity for 4R-tau aggregates. We also sought to improve brain penetrance, as dynamic PET imaging with [18F]CBD-2115 was conducted in mice, rats, and nonhuman primates, and all species showed initial brain uptake of 0.5−0.65 standardized uptake value (SUV) with fast

clearance from normal tissues. Herein, we describe our efforts using in silico methods to identify new lead 4R-tau ligands.

RESULTS AND DISCUSSSION

This study examined a variety of in silico approaches geared toward the identification of ligands for non-AD tauopathies. Given the recently disclosed cryo-EM structure identifying the binding site of PM-PBB3 within AD-tau filaments, we considered the possibility that CBD-2115 may also bind these sites.[39] Although the cryo-EM structures of AD and non-AD tau filaments show distinct structures, there may be common features found within their small-molecule binding sites. This could enable the application of structure-based in silico methods such as docking to identify a novel chemical matter with sufficient affinity to be useful as a PET radioligand.[40] We interrogated this line of reasoning by conducting a series of cross-competition binding experiments with PM-PBB3 and CBD-2115 in post-mortem tissues, including AD, PSP, and CBD tissues (Table 1). CBD-2115 was unable to effectively displace [3H]PM-PBB3 at concentrations of up to 10 μM, indicating that these ligands do not share overlapping high affinity binding sites. This was further supported with the similar observation that PM-PBB3 was unable to displace [3H]CBD-2115 in these tissues up to 10

Table 1. Inhibition Constant (K_i) Values (n = 1) of Unlabeled CBD-2115 and PM-PBB3 and Their Radioligands in AD, PSP, and CBD Brain Homogenates

radioligand	competitor	AD tissue K_i (nM)	PSP tissue K_i (nM)	CBD tissue K_i (nM)
[3H]PM-PBB3	CBD-2115	7140	>10,000	2930
[3H]CBD-2115	PM-PBB3	7930	>10,000	1540

μM. This result is noteworthy, as it suggests that there exist at least two distinct binding sites on 4R-tau filaments found in PSP and CBD. In the case of PM-PBB3, the binding sites identified in the cryo-EM structure of PM-PBB3 were not predicted using *in silico* methods.[39] Given this precedent and the lack of observed displacement in cross-competition binding experiments, it was judged likely that further experimental efforts would be required to identify the binding site(s) of CBD-2115. As a result, we had low confidence that a structure-based *in silico* approach would enable us to identify novel high affinity ligands.

As a result of the absence of structural information surrounding the binding site of CBD-2115, we considered the use of a ligand-based *in silico* method for the identification of potential leads.[41] Previous structure−activity relationship (SAR) studies that led to the development of the AD-tau PET radiotracers [18F]JNJ-067 and [18F]PI-2620 showed that the addition and variation of heterocyclic nitrogen positions within the core of their respective lead compounds could significantly impact potency and selectivity.[42,43] We hypothesized that a similar variation of the heterocyclic nitrogens found in CBD-2115 could play an important role in the optimization of the affinity for tau. This led us to consider virtual screening approaches that would identify hit compounds with a core similar to CBD-2115, but with additional nitrogens within the aromatic rings. While this approach could sacrifice the potential novelty of chemical matter identified during our virtual screen, it would likely enrich the possibility for finding active compounds, as the identified hits might reveal additional details about the SAR of CBD-2115. As a result, we opted to use a chemical-fingerprint-based method to identify closely related compounds to CBD-2115 from virtual screening libraries.

The *in silico* search was initiated by constructing a high-resolution structural fingerprint database of a 3.5B compound library from the Enamine REAL collection. Our in-house software for fingerprint searches, molbeam, utilized RDKit Morgan fingerprints (radius = 2; 4096 bit) to describe compounds found within the library and employed an approach that relied on the minimization of Jaccard distance to identify promising leads.[44,45] The top 750 compounds were subjected to visual inspection and resulted in the identification of Z3777013540 (1-(5-(6-fluoro-1*H*-indol-2-yl)pyrimidin-2-yl)piperidin-4-ol, **1**), a compound that bears structural similarity to CBD-2115 and varies the position of heterocyclic nitrogens found within its core (Figure 1). In addition to similarity, two scoring methods (CNS MPO and BBB) for predicting brain penetrance were used to compare **1** to CBD-2115.[46,47] Given the more favorable CNS MPO scores (3.7 for CBD-2115 vs 3.8 for **1**), CNS PET MPO scores (1.9 for CBD-2115 vs 2.8 for **1**), and BBB scores (3.18 for CBD-2115 vs 3.55 for **1**) relative to CBD-2115, we opted to evaluate **1** as a potential lead.[38,46] The improved predictive scores for brain uptake by all three calculations for **1** over CBD-2115 were primarily attributed to a decreased number of hydrogen bond donors. Disappointingly, **1** showed poor displacement of [3H]CBD-2115 in AD, PSP, and CBD brain tissue (Table 2). To our surprise, the evaluation of **1** against [3H]PM-PBB3 revealed low nM K_i values in AD, PSP, and CBD brain tissues (Table 2). This result was unexpected, as our initial cross-competition binding studies demonstrated that PM-PBB3 and CBD-2115 do not share a common high affinity binding site (Table 1). The primary structural differences between **1** and

Table 2. Inhibition Constant (K_i) Values ($n = 1$) of Unlabeled 1 and Tau Radioligands in AD, PSP, and CBD Brain Homogenates

radioligand	competitor	AD tissue K_i (nM)	PSP issue K_i (nM)	CBD issue K_i (nM)
[3H]PM-PBB3	**1**	18	20	22
[3H]CBD-2115	**1**	270	250	210
[3H]PI-2620	**1**	80	95	71

CBD-2115 include the substitution pattern on the indole (5-OH to 6-F), B-ring (pyridinyl to pyrimidinyl), and truncation of a methylene in the 4-piperidine substituent. Together, these modifications resulted in a remarkable shift in binding site selectivity toward displacement of PM-PBB3. Although this result was unforeseen, we further sought to characterize the *in vitro* binding properties of **1** in AD, PSP, and CBD brain tissue.

Tritium labeling of **1** was conducted by a commercial vendor (Novandi AB, Södertälje Sweden) through Ir-catalyzed hydrogen-tritium exchange, resulting in a high molar activity of [3H]**1** (2.72 GBq/μmol). Homologous binding assays with [3H]**1** in AD, PSP, and CBD brain tissue homogenates revealed low nM K_D values (Table 3). In addition, binding assays with [3H]**1** in PiD and Parkinson's disease (PD) homogenates revealed relatively high affinity of the radioligand to the PiD brain and low affinity to the PD brain containing α-synuclein aggregates (Table 3).

Additional binding assays were conducted in AD tissue homogenates to assess the affinity of **1** in competition with [3H]PiB binding to aggregated amyloid-beta (Aβ). The K_i of **1** versus [3H]PiB in AD tissue was 142 ± 5 nM ($n = 3$, mean + SD), indicating a relatively poor affinity of **1** for the PiB binding site on aggregated Aβ.

Next, we profiled a variety of tau tracers in competition binding studies with [3H]**1** to gain further insights into its binding site (Table 4). CBD-2115, MK-6240, and Tauvid revealed less effective competition in AD and PSP tissues compared to PM-PBB3. The relatively high K_i values observed with CBD-2115, MK-6240, and Tauvid support the notion that the high affinity binding site of **1** is largely distinct from those of these ligands. The use of PI-2620, a mixed 3R/4R- and 4R-tau agent, revealed high double-digit nanomolar K_i values in AD and PSP tissue. Given the observed K_i values, it is possible that PI-2620 shares some overlap in binding with **1**. Next, we profiled PM-PBB3 versus [3H]**1** in AD and PSP tissues and observed low nanomolar K_i values, indicating that these ligands share overlap in their binding sites. This observation is consistent with the K_i values obtained when **1** was competing against [3H]PM-PBB3 in AD and PSP tissue (Table 2). Taken together, **1** and PM-PBB3 appear to share similar binding sites with comparable affinity, suggesting that **1** may prove useful as a lead compound for the identification of ligands that bind the PM-PBB3 binding site.

We next turned our attention toward conducting initial SAR studies with the goal of improving the binding affinity. We utilized the SmallWorld similarity search (https://sw.docking.org) to identify a range of compounds that shared structural similarity with **1** within the Enamine REAL collection (22Q1) and focused on compounds modifying the indole core. Generally, compounds were picked from a pool that provided variation of the 6-fluoroindole core and maintained a similarity distance of less than 5. Our search revealed approximately 20 compounds with close structural similarity, and 17 were

Table 3. Equilibrium Dissociation Constant (K_D) and Maximum Binding Density (B_{max}) Values ($n = 3$; Mean $\pm$ SD) of [^{3}H]1 in AD, PSP, CBD, PiD, and PD Brain Homogenates

radioligand	AD tissue		PSP tissue		CBD tissue		PiD tissue		PD tissue	
	K_D (nM)	B_{max} (nM)	K_D (nM)	B_{max} (nM)	K_D (nM)	B_{max} (nM)	K_D (nM)	B_{max} (nM)	K_D (nM)	B_{max} (nM)
[^{3}H]1	4.0 $\pm$ 3.1	520 $\pm$ 370	5.1 $\pm$ 1.2	310 $\pm$ 90	4.5 $\pm$ 0.4	270 $\pm$ 40	9.7 $\pm$ 7.4	190 $\pm$ 100	89 $\pm$ 10	140 $\pm$ 50

Table 4. Inhibition Constant (K_i) Values ($n = 1$) of [^{3}H]1 and Prototypical Tau Ligands in AD and PSP Brain Homogenates

radioligand	competitor	AD tissue K_i (nM)	PSP tisue K_i (nM)
[^{3}H]1	PM-PBB3	15	18
[^{3}H]1	CBD-2115	745	520
[^{3}H]1	PI-2620	58	89
[^{3}H]1	MK-6240	96	315
[^{3}H]1	Tauvid	>1000	>1000

obtained commercially. The Tanimoto similarity scores (RDKit Morgan fingerprints, 1024 bit, radius = 2) between the selected compounds and 1/CBD-2115 were also calculated and indicated the selected compounds show low similarity to CBD-2115 (Table S2). Given the relative scarcity of well-characterized, copathology free AD and PSP tissues, compounds were initially triaged through a single-point screen at 300 nM concentration of unlabeled test compound versus [^{3}H]1. For compounds showing >65% displacement of [^{3}H]1, full competition binding curves were then determined.

Table 5. Effect on Binding Affinity of Varying the 6-Fluoro-indole Group of 1[a]
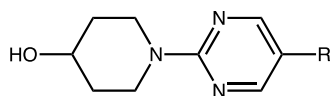
cpd	R	% of bound @ 300 nM AD Brain	% of bound @ 300 nM PSP Brain	cpd	R	% of bound @ 300 nM AD Brain	% of bound @ 300 nM PSP Brain
Z5555972024 **2**		64	76	Z2998207028 **11**		52	72
Z3790652493 **3**		37	59	Z3777013334 **12**		66	78
Z3347399002 **4**		49	63	Z3505916830 **13**		88	93
Z4387103711 **5**		48	68	Z5555971761 **14**		61	76
Z2739855509 **6**		20	32	Z2723085787 **15**		48	63
Z3831636212 **7**		85	92	Z2905421695 **16**		75	89
Z3505917044 **8**		92	97	Z2905421723 **17**		47	66
Z2905421604 **9**		67	88	Z3347398375 **18**		55	66
Z3831636329 **10**		56	66				

[a]Single concentration (300 nM) screening assay of Z-compounds vs [^{3}H]1 in AD and PSP brain homogenates ($n = 1$). Values shown are % bound [^{3}H]1 remaining vs 300 nM Z-compounds (smaller % remaining indicates greater competition).
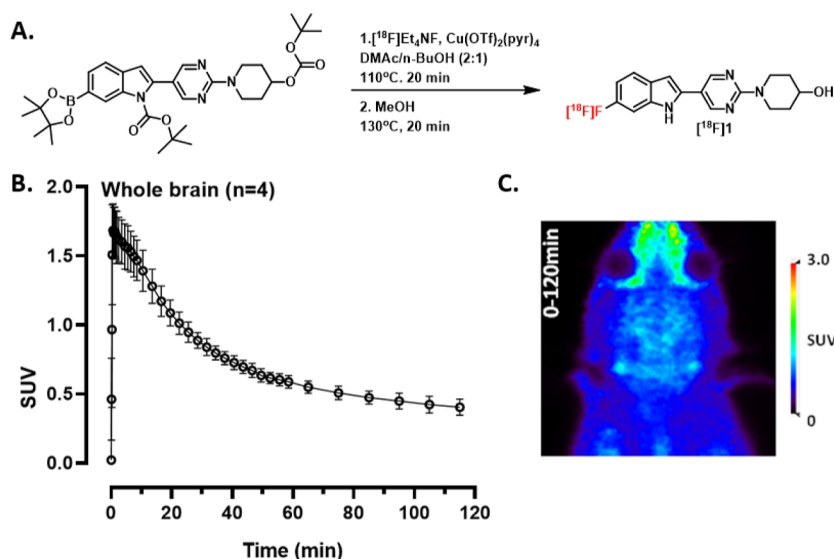
Figure 2. (A) Radiolabeling of $[^{18}F]$**1**. (B) Whole brain time activity curve (mean ± SD) of $[^{18}F]$**1** in rats ($n = 4$, 2F/2M). (C) PET summation image of the entire acquisition (0−120 min).

Evaluation of various replacements for the indole moiety on **1** was generally not favorable (Table 5). Some activity could be retained in both AD and PSP tissue when aza-indoles or triazolopyrimidine was utilized (**2**−**4**), although they did not reach the specified cutoff. More encouraging results were seen with benzothiophene derivatives, with 4-hydroxy-benzothiophene (**6**) displaying >65% inhibition of $[^{3}H]$**1** in both AD and PSP tissues. This activity was completely lost when moving from a benzothiophene core to a benzothiazole or azabenzothiazole (**7** and **8**). Similarly, compounds **8** and **9** showed a decrease in activity. Additionally, we examined a series of quinoline and isoquinoline derivatives (**11**−**13**), but generally found a loss of activity in PSP tissue. Finally, evaluation of substituted five-membered heterocycles including pyrazole (**15**), imidazole (**16** and **17**), and thiazole (**18**) revealed a substantial loss in activity in both AD and PSP tissues. Taken together, the results indicate that the binding affinity of **1** is strongly dependent on the presence of the 6-fluoro-indole core or electron-rich benzothiophenes. Following our initial screen, we selected benzothiophene compound **6** for further profiling. Competition binding assays with **6** versus $[^{3}H]$**1** revealed modest potency in AD (K_i = 12 nM; n = 1) and PSP homogenates (K_i = 22 nM; n = 1), respectively.

In addition to SAR studies, we conducted preliminary PET imaging studies with $[^{18}F]$**1** in rats. Although these preliminary imaging studies may not be translatable to nonhuman primates or humans, they give an early look at whether $[^{18}F]$**1** is brain penetrant or prone to defluorination. Furthermore, the study may also give an indication of whether $[^{18}F]$**1** could have off-target binding. $[^{18}F]$**1** was synthesized twice in nonoptimized radiochemical yield (RCY) of ∼0.5%, 99% radiochemical purity (RCP) and molar activities (A_m) of 46.1 and 47.2 GBq/μmol using alcohol-enhanced copper-mediated radiofluorination (Figure 2A).[48] Although unclear, a potential reason for the poor RCY could include protodeboronation of the starting material.[49] The log $D_{7.4}$ of $[^{18}F]$**1** was measured using the shake-flask procedure to 3.36 ± 0.04, which is within the upper range of known brain penetrant PET radiotracers.[50,51] Dynamic PET imaging was performed in four healthy wild-type (wt) rats. Following bolus intravenous (i.v.) admin-

istration of $[^{18}F]$**1**, radioactivity in the whole brain reached an initial maximum of 1.7 ± 0.2 standardized uptake value (SUV) within 5 min of injection and decreased to 0.4 SUV by the end of the 120 min PET scan (Figure 2B,C). The results indicate that $[^{18}F]$**1** is brain-penetrating and shows reasonable clearance from the brain over the course of the scan.

In an effort to identify more potent 4R-tau ligands than **1**, an additional chemical fingerprint search using **1** as the query of the Enamine REAL library was conducted and revealed three promising compounds that competed well with both $[^{3}H]$**1** and $[^{3}H]$PM-PBB3 in AD and PSP tissues (Table 6). The

Table 6. Inhibition Constant (K_i) Values (n = 1) of $[^{3}H]$1 vs Three Z-Compounds in AD and PSP Brain Homogenates[a]

Radioligand	Competitor	AD tissue K_i (nM)	PSP tissue K_i (nM)
$[^{3}H]$1	**19**	21	22
$[^{3}H]$1	**20**	18	18
$[^{3}H]$1	**21**	11	14

[a]Compounds **19** (Z5555972217), **20** (Z5555971887), and **21** (Z4169252340) are a promising second series of *in silico* molecular similarity search leads.

most potent of these was Z4169252340 (4-(5-(6-fluoro-1*H*-indol-2-yl)pyrimidin-2-yl)morpholine; **21**), which was tritiated using Ir-catalyzed hydrogen-tritium exchange, resulting in high molar activity $[^{3}H]$**21** (1.92 GBq/μmol).

Binding assays with $[^{3}H]$**21** in tissue homogenates provided K_D and nominal B_{max} values in AD, PSP, CBD, PiD, and PD tissues (Table 7). K_D values in AD, PSP, and CBD tissues approached 1 nM, while those in PiD and PD tissues were considerably higher. Additional binding assays were conducted in AD tissue homogenates to assess the affinity of **21** in competition with $[^{3}H]$PiB binding to aggregated Aβ. The K_i of **21** versus $[^{3}H]$PiB in AD tissue was 62 ± 3 nM (n = 3; mean ± SD), indicating a relatively low affinity of **21** for the PiB binding site on aggregated Aβ.

Table 7. Equilibrium Dissociation Constant (K_D) and Maximum Binding Density (B_{max}) Values ($n = 3$; Mean $\pm$ SD) of [³H]21 in AD, PSP, CBD, PiD, and PD Brain Homogenates

	AD tissue		PSP tissue		CBD tissue		PID tissue		PD tissue	
radioligand	K_D (nM)	B_{max} (nM)	K_D (nM)	B_{max} (nM)	K_D (nM)	B_{max} (nM)	K_D (nM)	B_{max} (nM)	K_D (nM)	B_{max} (nM)
[³H]21	1.2 ± 0.5	490 ± 280	1.6 ± 0.2	260 ± 70	1.7 ± 0.3	210 ± 50	10.3 ± 4.2	150 ± 80	140 ± 60	290 ± 170

We next determined the potency of **21** to compete with three tau tracers (Table 8). As was observed with **1**, compound

Table 8. Inhibition Constant (K_i) Values ($n = 1$) of 21 and Tau Radioligands in AD, PSP, and CBD Brain Homogenates

		AD tissue	PSP tissue	CBD tissue
radioligand	competitor	K_i (nM)	K_i (nM)	K_i (nM)
[³H]PM-PBB3	**21**	22	18	19
[³H]CBD-2115	**21**	270	270	230
[³H]PI-2620	**21**	100	93	110

21 competed well with [³H]PM-PBB3 in AD, PSP, and CBD tissues and less avidly with [³H]PI-2620 and [³H]CBD-2115. Hence, **21** and PM-PBB3 appear to share similar binding sites in AD, PSP, and CBD tissues, suggesting that **21** may prove useful, along with **1**, as a lead compound for the identification of ligands that bind the PM-PBB3 binding site.

The radiosynthesis of [¹⁸F]**21** was successfully carried out twice in nonoptimized of <1% RCY, 99% RCP and had A_m of 70.3 and 69.2 GBq/μmol using the same alcohol-enhanced copper-mediated radiofluorination employed for the synthesis of [¹⁸F]**1** (Figure 3A).[48] Although unclear, a potential reason for the poor RCY could include protodeboronation of the starting material.[49] The log $D_{7.4}$ of [¹⁸F]**21** was measured using the shake-flask procedure to 3.42 ± 0.08, which as expected is higher than [¹⁸F]**1** but also within the upper range of known brain penetrant PET radiotracers.[50,51] Dynamic PET imaging was performed in four healthy wild-type rats. Following bolus i.v. administration of [¹⁸F]**21**, radioactivity in the whole brain reached an initial maximum of 2.8 ± 0.15 SUV within 5 min of injection and decreased to 0.5 SUV by the end of the 120 min

PET scan (Figure 3B,C). The results indicate that [¹⁸F]**21** is brain penetrant and shows reasonable clearance from the brain during the course of the scan. Accumulation of radioactivity in bone tissue was observed during the PET scan reaching a maximum of 1.9 SUV after 120 min (Figure 3C), which could be a sign of defluorination and formation of free [¹⁸F]fluoride.

In summary, a chemical fingerprint similarity search was conducted within the Enamine REAL collection to identify compounds selective for 4R-tau that would overcome the limitations associated with CBD-2115. These searches identified **1** and **21**, which showed remarkable shifts in binding site preference toward the PM-PBB3 binding site found on tau filaments in AD, PSP, and CBD brain tissues. These outcomes were unexpected, as PM-PBB3 and CBD-2115 bind different sites on tau filaments. Tissue binding studies carried out with [³H]**1** and [³H]**21** indicated that their affinities (K_D) in AD, PSP, and CBD tissues were in the low nM range. This is notable because PM-PBB3 and related compounds possess a butadiene moiety that is ambient light sensitive, making its use for routine clinical imaging and high-throughput screening challenging.[52,53] Following the discovery of **1**, we conducted initial SAR studies that focused on replacing the 6-fluoro-indole core, leading to the discovery of **6**, which features a 4-hydroxy-benzothiophene. While **6** does not significantly improve upon the affinity of **1**, it demonstrates that the 6-fluoro-indole core can be substituted with different heterocycles.

Future work could further expand upon these observations and aim toward the discovery of even higher affinity 4R-tau ligands. Furthermore, **1** and **21** could be useful probes for supporting the identification of small-molecule binding sites on 4R-tau aggregates with cryo-EM. This may enable structure-based efforts to improve the affinity and selectivity of these
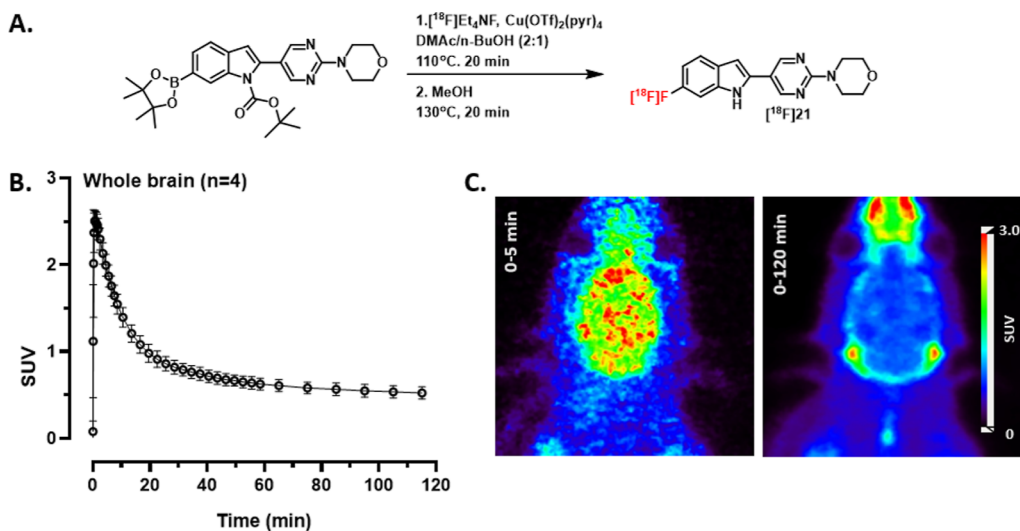

Figure 3. (A) Radiolabeling of [¹⁸F]**21**. (B) Whole brain time activity curve (mean $\pm$ SD) of [¹⁸F]**21** in rats ($n = 4$, 2F/2M). (C) PET summation images from rat PET scans using [¹⁸F]**21** from 0 to 5 and 0−120 min. The first panel shows initial brain uptake, while the second panel shows likely skull uptake occurring over 120 min.

compounds and provide useful models for virtual screening methods such as docking. In addition to extensive *in vitro* characterization, preliminary PET imaging studies with [^{18}F]**1** and [^{18}F]**21** indicated that the radioligands have favorable brain penetration and clearance in rats. This supports our observation that both **1** and **21** possessed improved CNS MPO and BBB scores relative to CBD-2115 and is attributed to decreased number of hydrogen bond donors. This encouraging observation suggests that related compounds may also possess similar BBB penetrance. Taken together, we anticipate that **1** and **21** will be of value in the discovery of additional radioligands targeting non-AD tauopathies.

■ EXPERIMENTAL SECTION

General. Animal studies were carried out in accordance with the guidelines put forth by the institutional animal care and use committees at CAMH. The purity of final products was determined by HPLC. All final products had a purity of ≥95%, unless noted otherwise. The unlabeled compounds in this study were obtained from the following vendors: PM-PBB3 (MedChem Imaging, Inc., USA); CBD-2115 (Oxiant Discovery AB and Novandi Chemistry AB, Sweden); PI-2620 (MedChem Imaging, Inc., USA); MK-6240 (Cerveau Technologies, USA); Tauvid (Huayi Isotopes Company, Canada); PiB (University of Pittsburgh, USA); compounds **1**−**21** were obtained from Enamine (see the Supporting Information for chemical purity); and precursors for [^{18}F]**1** and [^{18}F]**21** were custom synthesized by a commercial vendor (MedChem Imaging, Inc., USA) in >95% purity (Figures S3 and S4).

Tritiated Radioligands. Tritium labeled compounds were custom-synthesized by a commercial vendor (Novandi Chemistry AB, Sweden) with a high RCP and A_m: [^{3}H]PM-PBB3: RCP 99% and A_m 2.63 ± 0.35 TBq/mmol (70.5 ± 9.5 Ci/mmol); [^{3}H]CBD-2115: RCP > 96% and A_m 1.21 ± 0.21 TBq/mmol (32.75 ± 6.02 Ci/mmol); [^{3}H]PI-2620: RCP > 97% and A_m 1.82 TBq/mmol (49 Ci/mmol); [^{3}H]PiB: RCP > 98% and A_m 3.01 and 3.03 TBq/mmol (81 and 82 Ci/mmol); [^{3}H]**1**: RCP > 99% and A_m 2.72 TBq/mmol (74 Ci/mmol); [^{3}H]**21**: RCP > 98% and A_m 1.95 TBq/mmol (53 Ci/mmol).

Fingerprint Similarity Search. Software utilized for conducting the fingerprint search is provided at https://github.com/abazabaaa/molbeam_fp. A test script is provided to demonstrate a fingerprint search on a small scale.

Post-Mortem Tissues. Post-mortem human brain tissues were collected by brain banks at the University of California, San Francisco (UCSF) and Banner/Sun Health AZ following informed consent of the donors and utilized at the University of Pittsburgh under the approval of the Committee for Oversight of Research and Clinical Training Involving Decedents (CORID no. 295). The binding assays utilized fresh frozen, autopsy-confirmed, post-mortem human AD, PSP, CBD, and PiD brain tissue blocks (1 cm^3) obtained from the Neurodegenerative Disease Brain Bank at UCSF, containing only frequent mixed 3R/4R-tau neurofibrillary tangles and amyloid-beta plaque aggregates (AD tissue middle frontal gyrus), or only 4R-tau aggregates (PSP tissue, superior frontal gyrus, or CBD tissue, middle frontal gyrus), or only 3R-tau aggregates (PiD tissue middle frontal gyrus) and no other detectable aggregated amyloid or TDP-43 species. Fresh frozen, autopsy-confirmed human PD anterior cingulate cortex brain tissue blocks (1 cm^3) were obtained from Dr. Thomas Beach at Banner/Sun Health AZ through the Michael J. Fox Foundation and contained frequent α-synuclein aggregates and no other detectable aggregated amyloid or TDP-43 species. The frozen tissue blocks were separately thawed and homogenized in ice-cold pH 7.0 phosphate-buffered saline (PBS) at 300 mg/mL on ice using a glass homogenizer, diluted 30-fold with PBS to 10 mg/mL and homogenized a second time with a Brinkmann Polytron homogenizer before storage at −80 °C. At the time of binding assays, frozen brain tissue homogenates were thawed to room temperature and diluted 10-fold in PBS to a concentration of 1 mg/mL.

***In Vitro* Competition (*K*$_i$) Assays.** The equilibrium inhibition constant (*K*$_i$) values of the unlabeled compounds were determined versus tritium-labeled radioligands using published methods.[54] Briefly, for non-Enamine compounds, the concentration of the unlabeled competitor compound (∼400 μM in the stock solution) was determined by quantitative NMR in DMSO-d_6 (0.25% DMSO in the final assay vials). The appropriate concentrations (ranging from 0.1 to 1000 nM) of unlabeled competitor in 400 μL of PBS buffer were combined with 500 μL of the tritium-labeled radioligand in PBS (∼1 nM final concentration of radioligand). For Enamine compounds **1**−**21**, the 10 mM stock solutions in DMSO were diluted to the appropriate concentrations (ranging from 0.1 to 1000 nM) of unlabeled competitor in 400 μL of PBS buffer and combined with 500 μL of the tritium-labeled radioligand in PBS (∼1 nM final concentration of radioligand). The assay was initiated by the addition of 100 μL of 1 mg/mL brain tissue homogenate to achieve a final concentration of 100 μg tissue/mL. After incubation for 60 min at room temperature, the binding mixture was filtered through a Whatman GF/B glass filter via a Brandel M-24R cell harvester (Gaithersburg, MD, USA) and rapidly washed four times with 3 mL of PBS buffer. The filters were counted in CytoScint-ES after thorough vortexing by using a liquid scintillation counter. Complete (100%) inhibition of specific binding was defined as the number of counts displaced by 1 μM unlabeled radioligand. All assays were performed in triplicate at each concentration.

Binding Affinity (*K*$_D$) Assays. Tritium-labeled radioligand binding assays utilized AD, PSP, CBD, PiD, or PD brain homogenates to determine equilibrium dissociation constant (*K*$_D$) values and were performed with minor modifications of the procedure previously described in detail.[55] The unlabeled test compound was dissolved in DMSO at 400 μM and then diluted to 20 μM with PBS to yield 5% DMSO/PBS. The remaining serial dilutions (typically from 6 μM to 4 nM) were made with 5% DMSO/PBS to maintain a constant DMSO concentration in the final assay. Fifty μL of these solutions was combined with 50 μL of tritiated test compound and 800 μL of PBS to yield 0.25% DMSO, ∼ 1 nM tritiated compound, and 0.2−1000 nM unlabeled compound in the final assay. The assay began by addition of 100 μL of the 1 mg/mL brain homogenate to achieve a final concentration of 100 μg tissue/mL. After incubation for 60 min at room temperature, the binding mixture was filtered through a Whatman GF/B glass filter via a Brandel M-24R cell harvester (Gaithersburg, MD) and rapidly washed three times with 3 mL of PBS. The filters were counted in CytoScint-ES after thorough vortexing and sitting overnight. All assays were performed at least in triplicate. The concentration of bound compound was determined from the radioactivity retained on the filter after correcting for the nondisplaceable radioactivity (defined as that remaining with ∼1 μM unlabeled compound) and the specific activity of the tritiated compound after dilution with varying concentrations of unlabeled compound. The *K*$_D$ value was determined by the slope (slope = −1/*K*$_D$) of a Scatchard plot of the bound/free versus bound radioligand values at the different ligand concentrations and the B_{max} value was determined by the *x*-axis intercept of the bound/free versus bound line.

Single Concentration Screening Assays. Screening assays of test compounds were conducted at a single concentration of 300 nM unlabeled competitor. The assay was conducted similarly as described for the determination of *K*$_i$ values, where no (0%) inhibition was defined by the number of counts specifically bound without the addition of any unlabeled competitor and complete (100%) inhibition was defined as the number of counts nonspecifically bound at 1 μM of the unlabeled radioligand. The % inhibition of the radioligand by the test compound at 300 nM was defined by the number of counts specifically bound at 300 nM divided by the difference of counts at 0% inhibition minus the counts at 100% inhibition multiplied by 100. All assays were performed in triplicate at each concentration.

Radiochemistry. For radiofluorination of [^{18}F]**1**, *tert*-butyl 2-(2-(4-((*tert*-butoxycarbonyl)oxy)piperidin-1-yl)pyrimidin-5-yl)-6-(4,4,5,5-tetramethyl-1,3,2-dioxaborolan-2-yl)-1*H*-indole-1-carboxylate was used as the precursor, and for radiolabeling of [^{18}F]**21**, *tert*-butyl

2-(2-morpholinopyrimidin-5-yl)-6-(4,4,5,5-tetramethyl-1,3,2-dioxaborolan-2-yl)-1H-indole-1-carboxylate was used as the precursor. Briefly, no-carrier added [^{18}F]F$^-$ was produced via the 18O(p,n)^{18}F reaction (Scanditronix MC-17 cyclotron) and transferred in [^{18}O] water to an automated commercial radiosynthesizer (GE TRACERlab FX2N) in a lead shielded hot cell. The [^{18}F]F$^-$ was trapped on a PS-HCO$_3$ ion exchange column (Chromafix) before being eluted with tetraethylammonium carbonate (5.2 mg, 18.6 μmol) in methanol (1 mL) in the reaction vessel. Solvents were evaporated under vacuum and subsequently azeotropically dried with acetonitrile (1 mL) under continuous nitrogen flow. The precursor (3 mg, 5 μmol) and tetrakis(pyridine)copper(II) triflate (8.5 mg 12 μmol), in dimethylacetamide (DMA) and butanol (8:2 v/v, 1 mL) was added and the reactor was heated to 80 °C for 20 min. The reactor was cooled down to 70 °C and methanol (2 mL) was added before heating to 130 °C for 20 min. The reactor was then cooled to 50 °C and the reaction mixture was diluted with acetonitrile/water (20:80) before being injected onto a reverse-phase HPLC column (LUNA 10 μm C18(2) 100 Å, 250 mm × 10 mm, Phenomenex). The desired product was eluted with a mobile phase of acetonitrile-NH$_4$CO$_2$H$_{aq}$ (0.05 M; 40/60, v/v) at a flow rate of 6 mL/min. The retention time of [^{18}F]**1** was 12−13 and 16 min for [^{18}F]**21**. The collected fraction was diluted with water (20 mL) and loaded onto a solid phase extraction (SPE) column (SepPak tC18, Waters). The SPE column was washed with water (10 mL) before the radiotracer was eluted by ethanol (1 mL) and mixed with sterile saline (9 mL). The purity and molar activity were determined by reverse-phase HPLC (InfinityLab Poroshell 120 PFP, 4.6 × 150 mm, 2.7 μm, Agilent) with UV and γ detector connected in series. The radiotracer was eluted with acetonitrile-NH$_4$CO$_2$H (0.05 M; 50/50, v/v) at a flow rate of 2 mL/min (retention time = 6 min for [^{18}F]**1** and 6.8 min for [^{18}F]**21**). Radiochemical identity was confirmed by coinjection of authentic standard with sample of final product formulation.

PET Imaging. Four healthy Sprague−Dawley rats (2 females, 2 males, 354.3 ± 69.4 g; 10 ± 5 months old) underwent 120 min dynamic PET imaging following the injection of [^{18}F]**1** (12.6 ± 4.25 MBq; A_m of 32 ± 14 GBq/μmol; mass injected of 1.2 ± 0.3 nmol/kg). Four healthy Sprague−Dawley rats (2 females, 2 males, 378.85 ± 98.62 g; 4 months old) underwent 120 min dynamic PET imaging following the injection of [^{18}F]**21** (18.84 ± 1.84 MBq; A_m of 47.7 ± 22.3 GBq/μmol; mass injected of 1.3 ± 0.6 nmol/kg). PET images were acquired by using a nanoScan PET/CT scanner (Mediso, Budapest, Hungary). The acquired list mode data were sorted into 39 frames (3 × 5, 3 × 15, 3 × 20, 7 × 60, 17 × 180, and 6 × 600 s) 3D true sinograms (ring difference 84). The 3D sinograms were converted into 2D sinograms using Fourier-rebinning and reconstructed by using a 2D-filtered back projection (FBKP) with a Hann filter at a cutoff of 0.50 cm^{-1}. A static image of the complete emission acquisition was reconstructed with the manufacturer's proprietary iterative 3D algorithm (six subsets and four iterations). All image data were corrected for detector geometry and efficiencies, dead-time and decay corrected to the start of acquisition, with corrections for attenuation and scatter using a CT-based material map. Image analyses and extraction of brain TACs from the dynamic FBKP images were performed using VivoQuant (2020patch1, Invicro) with standard MR brain template and atlas for rats.[56] SUV was calculated by normalizing the regional radioactivity for injected radioactivity and body weight of the animal.

ASSOCIATED CONTENT

Ⓢ Supporting Information

The Supporting Information is available free of charge at https://pubs.acs.org/doi/10.1021/acs.jmedchem.3c00775.

> SMILES strings for all compounds tested in this paper and their reported results (CSV)

> Purity of compounds **1−21**, purity of the precursors for [^{18}F]**1** and [^{18}F]**21**, and radio-HPLC traces for [^{18}F]**1** and [^{18}F]**21** (PDF)

AUTHOR INFORMATION

Corresponding Author

Thomas J. A. Graham − *Department of Radiology, University of Pennsylvania, Philadelphia, Pennsylvania 19104-6323, United States;* Present Address: Molder Center for Drug Discovery Research, Temple University School of Pharmacy, Philadelphia, Pennsylvania 19140, United States; ⓞ orcid.org/0000-0002-3733-4106; Phone: +1 267 879 7012; Email: thomas.j.a.graham@gmail.com, thomas.graham@temple.edu

Authors

Anton Lindberg − *Azrieli Centre for Neuro-Radiochemistry, Brain Health Imaging Centre, Centre for Addiction and Mental Health, Toronto, Ontario M5T 1R8, Canada*

Junchao Tong − *Azrieli Centre for Neuro-Radiochemistry, Brain Health Imaging Centre, Centre for Addiction and Mental Health, Toronto, Ontario M5T 1R8, Canada*

Jeffrey S. Stehouwer − *Department of Radiology, University of Pittsburgh, Pittsburgh, Pennsylvania 15213, United States;* ⓞ orcid.org/0000-0001-8871-2544

Neil Vasdev − *Azrieli Centre for Neuro-Radiochemistry, Brain Health Imaging Centre, Centre for Addiction and Mental Health, Toronto, Ontario M5T 1R8, Canada; Department of Psychiatry, University of Toronto, Toronto, Ontario M5T 1R8, Canada;* ⓞ orcid.org/0000-0002-2087-5125

Robert H. Mach − *Department of Radiology, University of Pennsylvania, Philadelphia, Pennsylvania 19104-6323, United States;* ⓞ orcid.org/0000-0002-7645-2869

Chester A. Mathis − *Department of Radiology, University of Pittsburgh, Pittsburgh, Pennsylvania 15213, United States*

Complete contact information is available at:
https://pubs.acs.org/10.1021/acs.jmedchem.3c00775

Author Contributions

T.J.A.G., N.V., R.H.M., and C.A.M. conceived this work and designed the experiments. T.J.A.G. wrote the software used for chemical fingerprint searches. T.J.A.G., A.L., J.T., and J.S.S. performed experiments and data analysis. T.J.A.G., N.V., R.H.M., and C.A.M. are PIs or Leaders of this project and contributed to manuscript preparation. All the authors contributed to this manuscript and approved the final version.

Notes

The authors declare the following competing financial interest(s): N.V. is a co-founder of MedChem Imaging, Inc., a contract research organization that synthesized the ^{18}F-labeling precursors. All other authors declare no competing financial interest.

by the Neurodegenerative Disease Brain Bank at the University of California, San Francisco, which receives funding support from NIH grants P30AG062422, P01AG019724, U01AG057195, and U19AG063911, the Rainwater Charitable Foundation, and the Bluefield Project to Cure FTD. Human PD tissue was provided by the Michael J. Fox Foundation.

ABBREVIATIONS

3R, three microtubule-binding repeats; 4R, four microtubule-binding repeats; Aβ, amyloid-beta; AD, Alzheimer's disease; BBB, blood−brain barrier; CBD, corticobasal degeneration; CTE, chronic traumatic encephalopathy; DVR, distribution volume ratio; i.v, intravenous; MPO, multiparameter optimization; PD, Parkinson's disease; PET, positron emission tomography; PiD, Pick's disease; PSP, primary supranuclear palsy; RCP, radiochemical purity; RCY, radiochemical yield; SAR, structure−activity relationship; SUV, standardized uptake value; SUVR, standardized uptake value ratio

REFERENCES

(1) Ballatore, C.; Lee, V. M.-Y.; Trojanowski, J. Q. Tau-Mediated Neurodegeneration in Alzheimer's Disease and Related Disorders. *Nat. Rev. Neurosci.* **2007**, *8*, 663−672.
(2) Goedert, M.; Eisenberg, D. S.; Crowther, R. A. Propagation of Tau Aggregates and Neurodegeneration. *Annu. Rev. Neurosci.* **2017**, *40*, 189−210.
(3) Berriman, J.; Serpell, L. C.; Oberg, K. A.; Fink, A. L.; Goedert, M.; Crowther, R. A. Tau Filaments from Human Brain and from *in Vitro* Assembly of Recombinant Protein Show Cross-β Structure. *Proc. Natl. Acad. Sci. U.S.A.* **2003**, *100*, 9034−9038.
(4) Arai, T.; Ikeda, K.; Akiyama, H.; Shikamoto, Y.; Tsuchiya, K.; Yagishita, S.; Beach, T.; Rogers, J.; Schwab, C.; McGeer, P. L. Distinct Isoforms of Tau Aggregated in Neurons and Glial Cells in Brains of Patients with Pick's Disease, Corticobasal Degeneration and Progressive Supranuclear Palsy. *Acta Neuropathol.* **2001**, *101*, 167−173.
(5) Sergeant, N.; Wattez, A.; Delacourte, A. Neurofibrillary Degeneration in Progressive Supranuclear Palsy and Corticobasal Degeneration. Tau Pathologies with Exclusively "Exon10" Isoforms. *J. Neurochem.* **1999**, *72*, 1243−1249.
(6) Greenberg, S. G.; Davies, P.; Schein, J. D.; Binder, L. I. Hydrofluoric Acid-Treated Tau PHF Proteins Display the Same Biochemical Properties as Normal Tau. *J. Biol. Chem.* **1992**, *267*, 564−569.
(7) Lee, V. M.-Y.; Balin, B. J.; Otvos, L.; Trojanowski, J. Q. A68: A Major Subunit of Paired Helical Filaments and Derivatized Forms of Normal Tau. *Science* **1991**, *251*, 675−678.
(8) Goedert, M.; Spillantini, M. G.; Cairns, N. J.; Crowther, R. A. Tau Proteins of Alzheimer Paired Helical Filaments: Abnormal Phosphorylation of All Six Brain Isoforms. *Neuron* **1992**, *8*, 159−168.
(9) McKee, A. C.; Stein, T. D.; Kiernan, P. T.; Alvarez, V. E. The Neuropathology of Chronic Traumatic Encephalopathy: CTE Neuropathology. *Brain Pathol.* **2015**, *25*, 350−364.
(10) Schmidt, M.; Zhukareva, V.; Newell, K.; Lee, V.; Trojanowski, J. Tau Isoform Profile and Phosphorylation State in Dementia Pugilistica Recapitulate Alzheimer's Disease. *Acta Neuropathol.* **2001**, *101*, 518−524.
(11) Falcon, B.; Zhang, W.; Schweighauser, M.; Murzin, A. G.; Vidal, R.; Garringer, H. J.; Ghetti, B.; Scheres, S. H. W.; Goedert, M. Tau Filaments from Multiple Cases of Sporadic and Inherited Alzheimer's Disease Adopt a Common Fold. *Acta Neuropathol.* **2018**, *136*, 699−708.
(12) Fitzpatrick, A. W. P.; Falcon, B.; He, S.; Murzin, A. G.; Murshudov, G.; Garringer, H. J.; Crowther, R. A.; Ghetti, B.; Goedert, M.; Scheres, S. H. W. Cryo-EM Structures of Tau Filaments from Alzheimer's Disease. *Nature* **2017**, *547*, 185−190.

(13) Falcon, B.; Zivanov, J.; Zhang, W.; Murzin, A. G.; Garringer, H. J.; Vidal, R.; Crowther, R. A.; Newell, K. L.; Ghetti, B.; Goedert, M.; Scheres, S. H. W. Novel Tau Filament Fold in Chronic Traumatic Encephalopathy Encloses Hydrophobic Molecules. *Nature* **2019**, *568*, 420−423.
(14) Shi, Y.; Zhang, W.; Yang, Y.; Murzin, A. G.; Falcon, B.; Kotecha, A.; van Beers, M.; Tarutani, A.; Kametani, F.; Garringer, H. J.; Vidal, R.; Hallinan, G. I.; Lashley, T.; Saito, Y.; Murayama, S.; Yoshida, M.; Tanaka, H.; Kakita, A.; Ikeuchi, T.; Robinson, A. C.; Mann, D. M. A.; Kovacs, G. G.; Revesz, T.; Ghetti, B.; Hasegawa, M.; Goedert, M.; Scheres, S. H. W. Structure-Based Classification of Tauopathies. *Nature* **2021**, *598*, 359−363.
(15) Falcon, B.; Zhang, W.; Murzin, A. G.; Murshudov, G.; Garringer, H. J.; Vidal, R.; Crowther, R. A.; Ghetti, B.; Scheres, S. H. W.; Goedert, M. Structures of Filaments from Pick's Disease Reveal a Novel Tau Protein Fold. *Nature* **2018**, *561*, 137−140.
(16) Zhang, W.; Tarutani, A.; Newell, K. L.; Murzin, A. G.; Matsubara, T.; Falcon, B.; Vidal, R.; Garringer, H. J.; Shi, Y.; Ikeuchi, T.; Murayama, S.; Ghetti, B.; Hasegawa, M.; Goedert, M.; Scheres, S. H. W. Novel Tau Filament Fold in Corticobasal Degeneration. *Nature* **2020**, *580*, 283−287.
(17) Scheres, S. H.; Zhang, W.; Falcon, B.; Goedert, M. Cryo-EM Structures of Tau Filaments. *Curr. Opin. Struct. Biol.* **2020**, *64*, 17−25.
(18) Groot, C.; Villeneuve, S.; Smith, R.; Hansson, O.; Ossenkoppele, R. Tau PET Imaging in Neurodegenerative Disorders. *J. Nucl. Med.* **2022**, *63*, 20S−26S.
(19) Beyer, L.; Brendel, M. Imaging of Tau Pathology in Neurodegenerative Diseases: An Update. *Semin. Nucl. Med.* **2021**, *51*, 253−263.
(20) Hostetler, E. D.; Walji, A. M.; Zeng, Z.; Miller, P.; Bennacef, I.; Salinas, C.; Connolly, B.; Gantert, L.; Haley, H.; Holahan, M.; Purcell, M.; Riffel, K.; Lohith, T. G.; Coleman, P.; Soriano, A.; Ogawa, A.; Xu, S.; Zhang, X.; Joshi, E.; Della Rocca, J.; Hesk, D.; Schenk, D. J.; Evelhoch, J. L. Preclinical Characterization of ^{18}F-MK-6240, a Promising PET Tracer for In Vivo Quantification of Human Neurofibrillary Tangles[18]F-MK-6240, a Promising PET Tracer for In Vivo Quantification of Human Neurofibrillary Tangles. *J. Nucl. Med.* **2016**, *57*, 1599−1606.
(21) Walji, A. M.; Hostetler, E. D.; Selnick, H.; Zeng, Z.; Miller, P.; Bennacef, I.; Salinas, C.; Connolly, B.; Gantert, L.; Holahan, M.; O'Malley, S.; Purcell, M.; Riffel, K.; Li, J.; Balsells, J.; OBrien, J. A.; Melquist, S.; Soriano, A.; Zhang, X.; Ogawa, A.; Xu, S.; Joshi, E.; Della Rocca, J.; Hess, F. J.; Schachter, J.; Hesk, D.; Schenk, D.; Struyk, A.; Babaoglu, K.; Lohith, T. G.; Wang, Y.; Yang, K.; Fu, J.; Evelhoch, J. L.; Coleman, P. J. Discovery of 6-(Fluoro-^{18}F)-3-(1H-pyrrolo[2,3-c]pyridin-1-yl)isoquinolin-5-amine ([18F]-MK-6240): A Positron Emission Tomography (PET) Imaging Agent for Quantification of Neurofibrillary Tangles (NFTs). *J. Med. Chem.* **2016**, *59*, 4778−4789.
(22) Pascoal, T. A.; Benedet, A. L.; Tudorascu, D. L.; Therriault, J.; Mathotaarachchi, S.; Savard, M.; Lussier, F. Z.; Tissot, C.; Chamoun, M.; Kang, M. S.; Stevenson, J.; Massarweh, G.; Guiot, M.-C.; Soucy, J.-P.; Gauthier, S.; Rosa-Neto, P. Longitudinal 18F-MK-6240 Tau Tangles Accumulation Follows Braak Stages. *Brain* **2021**, *144*, 3517−3528.
(23) Cho, H.; Choi, J. Y.; Lee, H. S.; Lee, J. H.; Ryu, Y. H.; Lee, M. S.; Jack, C. R.; Lyoo, C. H. Progressive Tau Accumulation in Alzheimer Disease: 2-Year Follow-up Study. *J. Nucl. Med.* **2019**, *60*, 1611−1621.
(24) Gogola, A.; Minhas, D. S.; Villemagne, V. L.; Cohen, A. D.; Mountz, J. M.; Pascoal, T. A.; Laymon, C. M.; Mason, N. S.; Ikonomovic, M. D.; Mathis, C. A.; Snitz, B. E.; Lopez, O. L.; Klunk, W. E.; Lopresti, B. J. Direct Comparison of the Tau PET Tracers ^{18}F-Flortaucipir and ^{18}F-MK-6240 in Human Subjects[18]F]Flortaucipir and [^{18}F]MK-6240 in Human Subjects. *J. Nucl. Med.* **2022**, *63*, 108−116.
(25) Xia, C.; Arteaga, J.; Chen, G.; Gangadharmath, U.; Gomez, L. F.; Kasi, D.; Lam, C.; Liang, Q.; Liu, C.; Mocharla, V. P.; Mu, F.; Sinha, A.; Su, H.; Szardenings, A. K.; Walsh, J. C.; Wang, E.; Yu, C.; Zhang, W.; Zhao, T.; Kolb, H. C. [18F]T807, a novel tau positron emission tomography imaging agent for Alzheimer's disease[18]F]T807,

a Novel Tau Positron Emission Tomography Imaging Agent for Alzheimer's Disease. *Alzheimer's Dementia* **2013**, *9*, 666−676.

(26) Aguero, C.; Dhaynaut, M.; Normandin, M. D.; Amaral, A. C.; Guehl, N. J.; Neelamegam, R.; Marquie, M.; Johnson, K. A.; El Fakhri, G.; Frosch, M. P.; Gomez-Isla, T. Autoradiography Validation of Novel Tau PET Tracer [F-18]-MK-6240 on Human Postmortem Brain Tissue. *Acta Neuropathol. Commun.* **2019**, *7*, 37.

(27) Lowe, V. J.; Curran, G.; Fang, P.; Liesinger, A. M.; Josephs, K. A.; Parisi, J. E.; Kantarci, K.; Boeve, B. F.; Pandey, M. K.; Bruinsma, T.; Knopman, D. S.; Jones, D. T.; Petrucelli, L.; Cook, C. N.; Graff-Radford, N. R.; Dickson, D. W.; Petersen, R. C.; Jack, C. R.; Murray, M. E. An Autoradiographic Evaluation of AV-1451 Tau PET in Dementia. *Acta Neuropathol. Commun.* **2016**, *4*, 58.

(28) Malarte, M.-L.; Nordberg, A.; Lemoine, L. Characterization of MK6240, a Tau PET Tracer, in Autopsy Brain Tissue from Alzheimer's Disease Cases. *Eur. J. Nucl. Med. Mol. Imaging* **2021**, *48*, 1093−1102.

(29) Marquié, M.; Normandin, M. D.; Meltzer, A. C.; Siao Tick Chong, M.; Andrea, N. V.; Antón-Fernández, A.; Klunk, W. E.; Mathis, C. A.; Ikonomovic, M. D.; Debnath, M.; Bien, E. A.; Vanderburg, C. R.; Costantino, I.; Makaretz, S.; DeVos, S. L.; Oakley, D. H.; Gomperts, S. N.; Growdon, J. H.; Domoto-Reilly, K.; Lucente, D.; Dickerson, B. C.; Frosch, M. P.; Hyman, B. T.; Johnson, K. A.; Gómez-Isla, T. Pathological Correlations of [F-18]-AV-1451 Imaging in Non-Alzheimer Tauopathies: Tau Imaging: Pathological Correlations. *Ann. Neurol.* **2017**, *81*, 117−128.

(30) Malarte, M.-L.; Gillberg, P.-G.; Kumar, A.; Bogdanovic, N.; Lemoine, L.; Nordberg, A. Discriminative Binding of Tau PET Tracers PI2620, MK6240 and RO948 in Alzheimer's Disease, Corticobasal Degeneration and Progressive Supranuclear Palsy Brains. *Mol. Psychiatry* **2023**, *28*, 1272−1283.

(31) Tagai, K.; Ono, M.; Kubota, M.; Kitamura, S.; Takahata, K.; Seki, C.; Takado, Y.; Shinotoh, H.; Sano, Y.; Yamamoto, Y.; Matsuoka, K.; Takuwa, H.; Shimojo, M.; Takahashi, M.; Kawamura, K.; Kikuchi, T.; Okada, M.; Akiyama, H.; Suzuki, H.; Onaya, M.; Takeda, T.; Arai, K.; Arai, N.; Araki, N.; Saito, Y.; Trojanowski, J. Q.; Lee, V. M. Y.; Mishra, S. K.; Yamaguchi, Y.; Kimura, Y.; Ichise, M.; Tomita, Y.; Zhang, M.-R.; Suhara, T.; Shigeta, M.; Sahara, N.; Higuchi, M.; Shimada, H. High-Contrast In Vivo Imaging of Tau Pathologies in Alzheimer's and Non-Alzheimer's Disease Tauopathies. *Neuron* **2021**, *109*, 42−58.e8.

(32) Li, L.; Liu, F.; Li, M.; Lu, J.; Sun, Y.; Liang, X.; Bao, W.; Chen, Q.; Li, X.; Zhou, X.; Guan, Y.; Wu, J.; Yen, T.; Jang, M.; Luo, J.; Wang, J.; Zuo, C. Clinical Utility of ^{18}F-APN -1607 Tau PET Imaging in Patients with Progressive Supranuclear Palsy^{18}F-APN-1607 Tau PET Imaging in Patients with Progressive Supranuclear Palsy. *Mov. Disord.* **2021**, *36*, 2314−2323.

(33) Brendel, M.; Barthel, H.; van Eimeren, T.; Marek, K.; Beyer, L.; Song, M.; Palleis, C.; Gehmeyr, M.; Fietzek, U.; Respondek, G.; Sauerbeck, J.; Nitschmann, A.; Zach, C.; Hammes, J.; Barbe, M. T.; Onur, O.; Jessen, F.; Saur, D.; Schroeter, M. L.; Rumpf, J.-J.; Rullmann, M.; Schildan, A.; Patt, M.; Neumaier, B.; Barret, O.; Madonia, J.; Russell, D. S.; Stephens, A.; Roeber, S.; Herms, J.; Bötzel, K.; Classen, J.; Bartenstein, P.; Villemagne, V.; Levin, J.; Höglinger, G. U.; Drzezga, A.; Seibyl, J.; Sabri, O. Assessment of ^{18}F-PI-2620 as a Biomarker in Progressive Supranuclear Palsy^{18}F-PI-2620 as a Biomarker in Progressive Supranuclear Palsy. *JAMA Neurol.* **2020**, *77*, 1408.

(34) Palleis, C.; Brendel, M.; Finze, A.; Weidinger, E.; Bötzel, K.; Danek, A.; Beyer, L.; Nitschmann, A.; Kern, M.; Biechele, G.; Rauchmann, B.; Häckert, J.; Höllerhage, M.; Stephens, A. W.; Drzezga, A.; Eimeren, T.; Villemagne, V. L.; Schildan, A.; Barthel, H.; Patt, M.; Sabri, O.; Bartenstein, P.; Perneczky, R.; Haass, C.; Levin, J.; Höglinger, G. U. German Imaging Initiative for Tauopathies (GII4T). Cortical [^{18}F]PI-2620 Binding Differentiates Corticobasal Syndrome Subtypes. *Mov. Disord.* **2021**, *36*, 2104−2115.

(35) Tezuka, T.; Takahata, K.; Seki, M.; Tabuchi, H.; Momota, Y.; Shiraiwa, M.; Suzuki, N.; Morimoto, A.; Nakahara, T.; Iwabuchi, Y.; Miura, E.; Yamamoto, Y.; Sano, Y.; Funaki, K.; Yamagata, B.; Ueda,

R.; Yoshizaki, T.; Mashima, K.; Shibata, M.; Oyama, M.; Okada, K.; Kubota, M.; Okita, H.; Takao, M.; Jinzaki, M.; Nakahara, J.; Mimura, M.; Ito, D. Evaluation of [^{18}F]PI-2620, a Second-Generation Selective Tau Tracer, for Assessing Four-Repeat Tauopathies. *Brain Commun.* **2021**, *3*, fcab190.

(36) Logan, J.; Fowler, J. S.; Volkow, N. D.; Wang, G.-J.; Ding, Y.-S.; Alexoff, D. L. Distribution Volume Ratios without Blood Sampling from Graphical Analysis of PET Data. *J. Cereb. Blood Flow Metab.* **1996**, *16*, 834−840.

(37) Kinahan, P. E.; Fletcher, J. W. Positron Emission Tomography-Computed Tomography Standardized Uptake Values in Clinical Practice and Assessing Response to Therapy. *Semin. Ultrasound CT MR* **2010**, *31*, 496−505.

(38) Lindberg, A.; Knight, A. C.; Sohn, D.; Rakos, L.; Tong, J.; Radelet, A.; Mason, N. S.; Stehouwer, J. S.; Lopresti, B. J.; Klunk, W. E.; Sandell, J.; Sandberg, A.; Hammarström, P.; Svensson, S.; Mathis, C. A.; Vasdev, N. Radiosynthesis, In Vitro and In Vivo Evaluation of [^{18}F]CBD-2115 as a First-in-Class Radiotracer for Imaging 4R-Tauopathies. *ACS Chem. Neurosci.* **2021**, *12*, 596−602.

(39) Shi, Y.; Murzin, A. G.; Falcon, B.; Epstein, A.; Machin, J.; Tempest, P.; Newell, K. L.; Vidal, R.; Garringer, H. J.; Sahara, N.; Higuchi, M.; Ghetti, B.; Jang, M.-K.; Scheres, S. H. W.; Goedert, M. Cryo-EM Structures of Tau Filaments from Alzheimer's Disease with PET Ligand APN-1607. *Acta Neuropathol.* **2021**, *141*, 697−708.

(40) Lionta, E.; Spyrou, G.; Vassilatis, D.; Cournia, Z. Structure-Based Virtual Screening for Drug Discovery: Principles, Applications and Recent Advances. *Curr. Top. Med. Chem.* **2014**, *14*, 1923−1938.

(41) Sliwoski, G.; Kothiwale, S.; Meiler, J.; Lowe, E. W. Computational Methods in Drug Discovery. *Pharmacol. Rev.* **2014**, *66*, 334−395.

(42) Kroth, H.; Oden, F.; Serra, A. M.; Molette, J.; Mueller, A.; Berndt, M.; Capotosti, F.; Gabellieri, E.; Schmitt-Willich, H.; Hickman, D.; Pfeifer, A.; Dinkelborg, L.; Stephens, A. Structure-Activity Relationship around PI-2620 Highlights the Importance of the Nitrogen Atom Position in the Tricyclic Core. *Bioorg. Med. Chem.* **2021**, *52*, 116528.

(43) Rombouts, F. J. R.; Andrés, J. I.; Ariza, M.; Alonso, J. M.; Austin, N.; Bottelbergs, A.; Chen, L.; Chupakhin, V.; Cleiren, E.; Fierens, K.; Fontana, A.; Langlois, X.; Leenaerts, J. E.; Mariën, J.; Martínez Lamenca, C.; Salter, R.; Schmidt, M. E.; Te Riele, P.; Wintmolders, C.; Trabanco, A. A.; Zhang, W.; Macdonald, G.; Moechars, D. Discovery of *N*-(Pyridin-4-yl)-1,5-naphthyridin-2-amines as Potential Tau Pathology PET Tracers for Alzheimer's Disease. *J. Med. Chem.* **2017**, *60*, 1272−1291.

(44) Landrum, G. *RDKit: Open-Source Cheminformatics*, 2006.

(45) Martin, L. J.; Bowen, M. T. Comparing Fingerprints for Ligand-Based Virtual Screening: A Fast and Scalable Approach for Unbiased Evaluation. *J. Chem. Inf. Model.* **2020**, *60*, 4536−4545.

(46) Wager, T. T.; Hou, X.; Verhoest, P. R.; Villalobos, A. Central Nervous System Multiparameter Optimization Desirability: Application in Drug Discovery. *ACS Chem. Neurosci.* **2016**, *7*, 767−775.

(47) Gupta, M.; Lee, H. J.; Barden, C. J.; Weaver, D. F. The Blood−Brain Barrier (BBB) Score. *J. Med. Chem.* **2019**, *62*, 9824−9836.

(48) Zischler, J.; Kolks, N.; Modemann, D.; Neumaier, B.; Zlatopolskiy, B. D. Alcohol-Enhanced Cu-Mediated Radiofluorination. *Chem.—Eur. J.* **2017**, *23*, 3251−3256.

(49) Mossine, A. V.; Brooks, A. F.; Bernard-Gauthier, V.; Bailey, J. J.; Ichiishi, N.; Schirrmacher, R.; Sanford, M. S.; Scott, P. J. H. Automated synthesis of PET radiotracers by copper-mediated ^{18}F-fluorination of organoborons: Importance of the order of addition and competing protodeborylation^{18}F-Fluorination of Organoborons: Importance of the Order of Addition and Competing Protodeborylation. *J. Labelled Compd. Radiopharm.* **2018**, *61*, 228−236.

(50) Wilson, A. A.; Jin, L.; Garcia, A.; DaSilva, J. N.; Houle, S. An Admonition When Measuring the Lipophilicity of Radiotracers Using Counting Techniques. *Appl. Radiat. Isot.* **2001**, *54*, 203−208.

(51) Waterhouse, R. Determination of Lipophilicity and Its Use as a Predictor of Blood−Brain Barrier Penetration of Molecular Imaging Agents. *Mol. Imaging Biol.* **2003**, *5*, 376−389.

(52) Hashimoto, H.; Kawamura, K.; Igarashi, N.; Takei, M.; Fujishiro, T.; Aihara, Y.; Shiomi, S.; Muto, M.; Ito, T.; Furutsuka, K.; Yamasaki, T.; Yui, J.; Xie, L.; Ono, M.; Hatori, A.; Nemoto, K.; Suhara, T.; Higuchi, M.; Zhang, M.-R. Radiosynthesis, Photo-isomerization, Biodistribution, and Metabolite Analysis of ^{11}C-PBB3 as a Clinically Useful PET Probe for Imaging of Tau Pathology[11]C-PBB3 as a Clinically Useful PET Probe for Imaging of Tau Pathology. *J. Nucl. Med.* **2014**, *55*, 1532−1538.

(53) Kawamura, K.; Hashimoto, H.; Furutsuka, K.; Ohkubo, T.; Fujishiro, T.; Togashi, T.; Arashi, D.; Sakai, T.; Muto, M.; Ogawa, M.; Kurihara, Y.; Nengaki, N.; Takei, M.; Nemoto, K.; Higuchi, M.; Zhang, M. Radiosynthesis and quality control testing of the tau imaging positron emission tomography tracer [[18] F]PM-PBB3 for clinical applications[18]F]PM-PBB3 for Clinical Applications. *J. Labelled Compd. Radiopharm.* **2021**, *64*, 109−119.

(54) Klunk, W. E.; Wang, Y.; Huang, G.; Debnath, M. L.; Holt, D. P.; Shao, L.; Hamilton, R. L.; Ikonomovic, M. D.; DeKosky, S. T.; Mathis, C. A. The Binding of 2-(4′-methylaminophenyl)-benzothiazole to Postmortem Brain Homogenates Is Dominated by the Amyloid Component. *J. Neurosci.* **2003**, *23*, 2086−2092.

(55) Klunk, W. E.; Wang, Y.; Huang, G.; Debnath, M. L.; Holt, D. P.; Mathis, C. A. Uncharged Thioflavin-T Derivatives Bind to Amyloid-Beta Protein with High Affinity and Readily Enter the Brain. *Life Sci.* **2001**, *69*, 1471−1484.

(56) Schwarz, A. J.; Danckaert, A.; Reese, T.; Gozzi, A.; Paxinos, G.; Watson, C.; Merlo-Pich, E. V.; Bifone, A. A Stereotaxic MRI Template Set for the Rat Brain with Tissue Class Distribution Maps and Co-Registered Anatomical Atlas: Application to Pharmacological MRI. *NeuroImage* **2006**, *32*, 538−550.